2021-02

Generation of a Conjoint Surface Plasmon by an Infrared NanoAntenna Array

Allsop, T

http://hdl.handle.net/10026.1/18858

RESEARCH ARTICLE

ADVANCED
PHOTONICS
RESEARCH
Open Access

www.adpr-journal.com

Generation of a Conjoint Surface Plasmon by an Infrared Nano-Antenna Array

Thomas Allsop,* Chengbo Mou,* Ronald Neal, Vojtěch Kundrát, Changle Wang, Kyriacos Kalli, David Webb, Xiaoping Liu, Paul Davey, Philip Culverhouse, and Juan Diego Ania-Castañón

Localized surface plasmons (LSP) excited by optical fields have many potential applications resulting from their ability in detecting ultra-small, ambient refractive index change. Current methods using surface nano-patterning by means of lithography have given rise to LSP of limited propagation and interaction lengths, meaning that practical applications remain challenging. This article describes a new all-optical method of generating LSP by means of a carefully fabricated low-dimensional nano-structured material using a direct-write photochemical lithography. It is shown that the resulting array of localized SPs combine or "Conjoin" to have an unprecedented large interaction length, via coupled evanescent fields, giving rise to superior spectral sensitivities; several orders of magnitude better than those quoted elsewhere and reaching 6×10^3 nm RIU^{-1} in the aqueous regime and 10^4 nm RIU^{-1} in the gaseous regime. Numerical modeling is performed that shows this design of plasmonic platform is capable of producing sensitivities of 10^5–10^6 nm RIU^{-1}. It is believed the results achieved in this investigation show that a unique conjoint SP operational mode will significantly impact areas of interest, such as single molecular dynamics, drug delivery systems, etc.

1. Introduction

Localized surface plasmons (LSPs) are damped collective free-electron oscillations, which can be generated on the surface of a nano-patterned metal when excited by electromagnetic radiation over a wide wavelength range. The field patterns of LSPs are extremely sensitive to optical parameters, such as changes in the refractive index (RI) surrounding the structured metal surface. This has led to intensive studies of the behavior of LSPs, with a view to exploiting their significant potential in various applications. For example, as sensors,[1] for surface-enhanced spectroscopy,[2] in photonic circuits,[3] within medical diagnostics/therapeutics and for monitoring real-time label-free biomolecular kinetics.[4,5] The LSPs exhibit low loss, high penetration depth, and a large spatially extended evanescent field. In the infrared spectrum, they are exploited in biological and molecular fingerprinting identification for medical diagnostics,[6]

Dr. T. Allsop, Dr. V. Kundrát, Dr. C. Wang, Prof. D. Webb
Aston Institute of Photonic Technologies (AIPT)
Aston University
Aston Triangle, Birmingham B4 7ET, UK
E-mail: t.allsop@hull.ac.UK

Dr. T. Allsop, Dr. J. Diego Ania-Castañón
Non-linear Dynamics and Fiber Optics, Consejo Superior de Investigaciones Científicas
Instituto de Óptica "Daza de Valdés" (IO-CSIC),
Calle de Serrano, 121, 28006 Madrid, Spain

Dr. T. Allsop
Faculty of Science and Engineering
University of Hull
Hull HU6 7RX, UK

Prof. C. Mou
Key Laboratory of Specialty Fiber Optics and Optical Access Network
Joint International Research Laboratory of Specialty Fiber Optics and Advanced Communication
Shanghai Institute for Advanced Communication and Data Science
Shanghai University
Shanghai 200444, China
E-mail: mouc1@shu.edu.cn

R. Neal, Dr. P. Davey, Dr. P. Culverhouse
School of Engineering, Computing and Mathematics, Faculty of Science and Technology
University of Plymouth
Plymouth PL4 8AA, UK

Prof. K. Kalli
Nanophotonics Research Laboratory
Department of Electrical Engineering, Computer Engineering and Informatics
Cyprus University of Technology
31 Archbishop Kyprianos, Lemessos 3036, Cyprus

Prof. X. Liu
School of Physical Science and Technology
ShanghaiTech University
Shanghai 201210, China

biochemistry, and environmental sensing.[7,8] More recently, researchers are beginning to see the potential important role for plasmonics in optoelectronics and telecommunications.[9,10]

It is well known that the dynamics of LSPs can be strongly influenced by subtle changes in the properties of any nano-patterned metal surface, e.g., surface roughness, rescattering losses, along with other losses from the conversion of the SPs into radiative bulk waves, leading to a prominent spectral shift of the LSPs resonances. Furthermore, the spatial distribution of the LSPs' evanescent field extends into the surrounding medium that defines their propagation and interaction length, and these two factors govern the spectral sensitivity of LSPs. To date, various types of surface patterns and geometries have been investigated to enhance LSPs' sensitivity, including nano-spheres and nano-wells.[11,12] There remains, however, one major obstacle the LSP propagation distance places a limit on the potential of having ultra-high spectral sensing sensitivities. To overcome this limitation, researchers since the 1970s have been investigating a myriad of surface structures, including metal nano-antennae to enhance the optical properties (including extending the propagation distance and the interaction length of the LSPs).[12] Furthermore, research into the properties of LSPs and their generation has gathered significant momentum in recent years,[13] because of the LSPs' quantum size effect resulting from discrete electron bands and the intrinsic ability to produce significantly stronger and confined electromagnetic fields supporting highly efficient LSP resonance.[14] These advances have led to applications, such as direct conversion of light to electrical power,[15] metamaterials,[16] optical switches,[13] and sensors.[17] The latter offers the abundant potential of low-cost sensing with 1 pm detection limits for certain bio-applications.[18] Nano-antenna devices are strong contenders as ultra-sensitive sensors.[19] The complexity in fabrication, however, currently hinders their development.[20,21]

In this work, we use a thin-film deposition technique (sputtering) followed by a direct-write UV-chemically induced geometric inscription technique to produce a large, long-range ordered array of nano-antennae on a composite film coated planar surface. We discover in our investigations that the fabricated plasmonic platforms create infrared LSP evanescent fields that overlap with the evanescent field generated by adjacent nano-antennae within the array; moreover, these fields are strongly coupled. This creates coupled evanescent fields from adjacent nano-antennae that spans over the entire array of the nano-antenna, thereby resulting in a "collective" evanescent field created by the individual nano-antenna within the array. This "collective field" can be visualized as a distinct mode of operation over the nano-antennae array, an assembly of LSP that can be thought of as a single conjoint SP. This new mode of operation of the SP are distinctively different from previously reported LSPs, whether they are conventional, damped, short-range, long-range, and localized. Furthermore, the nano-antennae within the array have long range repeatability on the order of 1 cm, thus the adjacent LSPs can couple to each other across the entire surface area of the nano-antenna array. Such long-range ordered nano-antennae array with mutually coupled LSPs produces an effective interaction length on a scale of few millimeters, which is two to three orders of magnitude higher than that of the conventional/typical LSP. Therefore, as the single

nano-antenna's LSPs is perturbed, this perturbation propagates across the nano-antennae array.

This distinctive feature leads to some of the highest spectral sensing sensitivities reported to date, exceeding 10^4 nm RIU^{-1} in the gaseous index regime and 6×10^3 nm RIU^{-1} in the aqueous index regime. First, experimental results presented in this article. Second, to explain the spectral behavior observed two modeling approaches have been used. To establish that these nano-antenna arrays produce LSPs resonances and the resonances polarization dependence as experimentally observed with these devices. We used a conventional analytical model that uses the measured dimensions of Pt nano-antennae array to calculate spectral location of resonances of LSPs. The analytical approach yields LSPs resonances in the same spectral location and predicts their tunability over a large spectral range for a single plasmonic device/sensor with polarization dependence. The issue with the analytical approach is that it fails to predict the experimental spectral index sensitivities. To predict these spectral index sensing sensitivities and to explain the mechanism that produces such high sensitivities, a second modeling approach using numerical finite element method (FEM) was implemented. The FEM model showed reasonable agreement with regard to sensing sensitivities. In addition, the FEM model produced data that was used to understand the mechanism behind the high sensitivities, through the mutually coupled LSPs by investigating the spatial extension of their evanescent fields generated by the SPs, which is perpendicular to the surface of the nano-antenna. These mutually coupled evanescent fields creates a homogenous field extending over the array of nano-antennae.

The findings reported here also show possibly new direction to achieve further sensitivity enhancement. The FEM modeling has shown that the spectral sensitivity can potentially reach ultra-high values up to 10^5–10^6 nm RIU^{-1} in the aqueous regime. The authors have already used this optical phenomenon, in conjunction with gold–thiol immobilized bio-recognition molecule, a bisphenol-A aptamer.[22] The combination of this optical platform working with this aptamer has produced a detection scheme capable of sensing the presence of small molecules. In this particular case, bishenol-A (size 228 Da), yielding a limit of detection (LOD) of 330 atto-molars.[22]

2. Results

The 2D nanostructured, optical–plasmonic platform devices exhibit a long-range order on the scale of ≈1 cm. This is realized in a two-stage process; step-one, the fabrication of a multi-layered thin film/coating on the supporting waveguide (studied using planar BK7 substrates and used with D-shaped single-mode optical fiber as the optical waveguide) are fabricated using RF sputtering machine. The sputtering machine deposited three different materials onto a supporting substrate/waveguide. These materials are thin films of germanium (48 nm), silicon dioxide (48 nm), and a metal over-lay coating that could be of various thicknesses, depending upon the metal used, which creates a planar structure. Step two, the fabrication of the 2D nanostructure produced by UV photo-bleaching;[23] this is a chemical reaction between UV irradiance and the germanium/germanium oxide. This is a standard reaction used to fabricate

Bragg gratings in optical fibers; more detail on the entire fabrication process steps is given in the Experimental Section of this article. There are two physical mechanisms occurring with regard to the illumination of the germanium material by UV radiation. First, a redox reaction occurring specifically at Ge=O/Ge—O bonds resulting in a change in the electron density that modifies the permittivity, and so the RI at that location. Second, the elasto-optic effect,[24] which creates additional changes to the RI in the material due to a "geometric spatial compaction" of the material itself, resulting in stress within the material. This "compaction" mechanism results in the physical formation of 2D nanostructures on the supporting substrate surface, from the initial planar metal (gold) overlay (prior to UV illumination) to a situation where the metal is located at the vertices of the corrugation, thereby creating metal (gold) nano-antennae surrounded by air and SiO_2 after the UV processing, (**Figure 1**). The net effect is the creation of an array of parallel gold nano-antennae on the surface, with a repeatable scale on the order of 1 cm.

Atomic force microscopic (AFM) measurements, shown in Figure 1a,b, reveal that the surface topology of the mechanically lapped and coated D-shaped fiber, after UV-irradiance through a phase mask.[25] The coating layers from bottom to top are germanium, silicon dioxide, and the metal overlay. The corresponding film thicknesses are inter-related and chosen to maximize the SP field; further details of the fabrication process are given in the Supporting Information. Noticeably, the surface features small striped elements (nano-antennae) with a mean width of 110 ± 10 nm and a typical length of 10 ± 0.5 µm. They form an array with a predominant period of 520 ± 10 nm and a typical array length of 1–2 cm.

The zoomed AFM image further reveals a twisted, rope-like nano-antenna structure with a defined orientation. Fast Fourier transform (FFT) analysis performed along an individual nano-antenna and on cross-sections between nano-antennas is shown in Figure 1c,d, respectively. It reveals fundamental periods of 0.54 µm and 1.02 µm across the corrugations, which is consistent with the 1.02 µm fundamental period of the phase mask used when irradiating with UV irradiance. The fundamental period along an individual antenna is 0.29 µm. It is the direct result of the focused UV-laser beam passing through the phase mask and generating a 3D fringe pattern on the sample.[25,26] The "twisted rope-like" shape is hence associated with the germanium on exposure to the highest UV light intensity. This pattern is more predominant if the fiber samples are not parallel to the phase mask. We noted that the planar BK7 glass with the same coating produces similar surface topological profiles to the aforementioned coated D-shaped fiber, as shown in Figure 1e,f. The length of a single nano-antenna in this case is ≈30 µm, with an overall scale of the patterned region of 2 cm. Furthermore, regularity/repeatability of the surface structures on the planar sample can be seen from a typical cross-sectional line profile of an AFM image in Figure 1f. A closer inspection of Figure 1f shows an envelope function in the amplitude/height of the surface corrugations. Performing a FFT on a typical cross-section line profile of an AFM map detected dominant harmonics with periods of 0.54, 1.02 and 1.54 µm, which suggests that there is mixing of residual zeroth order with the ±1st orders of the phase mask causing multiple beam mixing. Figure 1g

shows the concept of the conjoined SPs, showing a typical LSP that is generated and propagates along individual nano-antenna within the array. In addition, Figure 1g shows the spatial extension of the perpendicular electric evanescent field generated by the SPs at the surface of the nano-antenna and that there is significant overlap between the electric field generated from a single nano-antenna to its adjacent nano-antenna.

We investigate first the LSP-induced polarization responsivity of the nano-patterned D-shaped fiber in air at room temperature and at 1 atm pressure, using the configuration shown in **Figure 2**. A broadband light source is linearly polarized and the polarization state of the light is controlled that is used to optically illuminate the sensing platform and its LSPs. The optical transmission spectra of the sensing platform which includes the excitation resonances of the LSP is monitored using an approach similar to a previous report.[25]

To measure the spectral index sensitivity of the LSP sensing platform, the D-shaped optical fiber is held in a V-groove on an aluminum plate mounted on an optical table that acts as a heat sink to maintain a constant temperature of 23 °C throughout the experiment, see Figure 2a. The LSP sensor is subsequently immersed in a series of certified RI liquids (Cargille–Sacher Laboratories Inc, quoted accuracy of ±0.0002). The low RI spectral sensitivity characterization is performed by a series of gas-exposure measurements using the alkane gases; these being methane, ethane, propane, and butane.

Each of these gases are delivered separately via a gas manifold to a sealed chamber having a total volume of 3 L (additional 2 L for feed and exhaust pipes) as shown in Figure 2b. More details of the characterization apparatus and procedure are given in the Supporting Information.

The typical optical spectral response of the sensing platform based upon the D-shaped fiber to the change of azimuthal polarization angle in air before and after UV-inscription, is shown in **Figure 3**. The maximum optical strength of the LSP resonance is defined as the maximum extinction band in the optical transmission spectra of the sensing platform. Note that before UV-irradiation, the three overlay coating on the D-shaped fiber only supports conventional SPs, whereas after the UV-inscription the corrugated nano-structures are capable of supporting LSPs. In our results, the zero azimuthal angle polarization is defined as the angle corresponding to the maximum optical coupling to the SPs, i.e., the minimum transmission optical power. It is known that the dispersion relation of the LSPs is different to that of conventional SPs. Furthermore, that the polarization sensitivity of LSPs is higher than that of conventional SPs. The results in Figure 3 show almost an order of magnitude increase in polarization sensitivity for the LSPs compared with the conventional SPs, from 1.0 to 7.3 nm degree^{-1} and the corresponding optical strength sensitivity is greatly enhanced, from 0.7 to 5.3 dB degree^{-1}, following the UV processing. We observe that when the azimuthal polarization angle is varied from 40° to 170°, both spectral and optical strength sensitivity is low; this is regardless of UV-laser processing; see the unshaded region of Figure 3.

The RI spectral sensitivity of the sensing platforms yields higher sensitivities for gaseous and liquid regimes after UV-laser processing. This is expected due to the change in the surface topology from a planar metal overlay to an array of
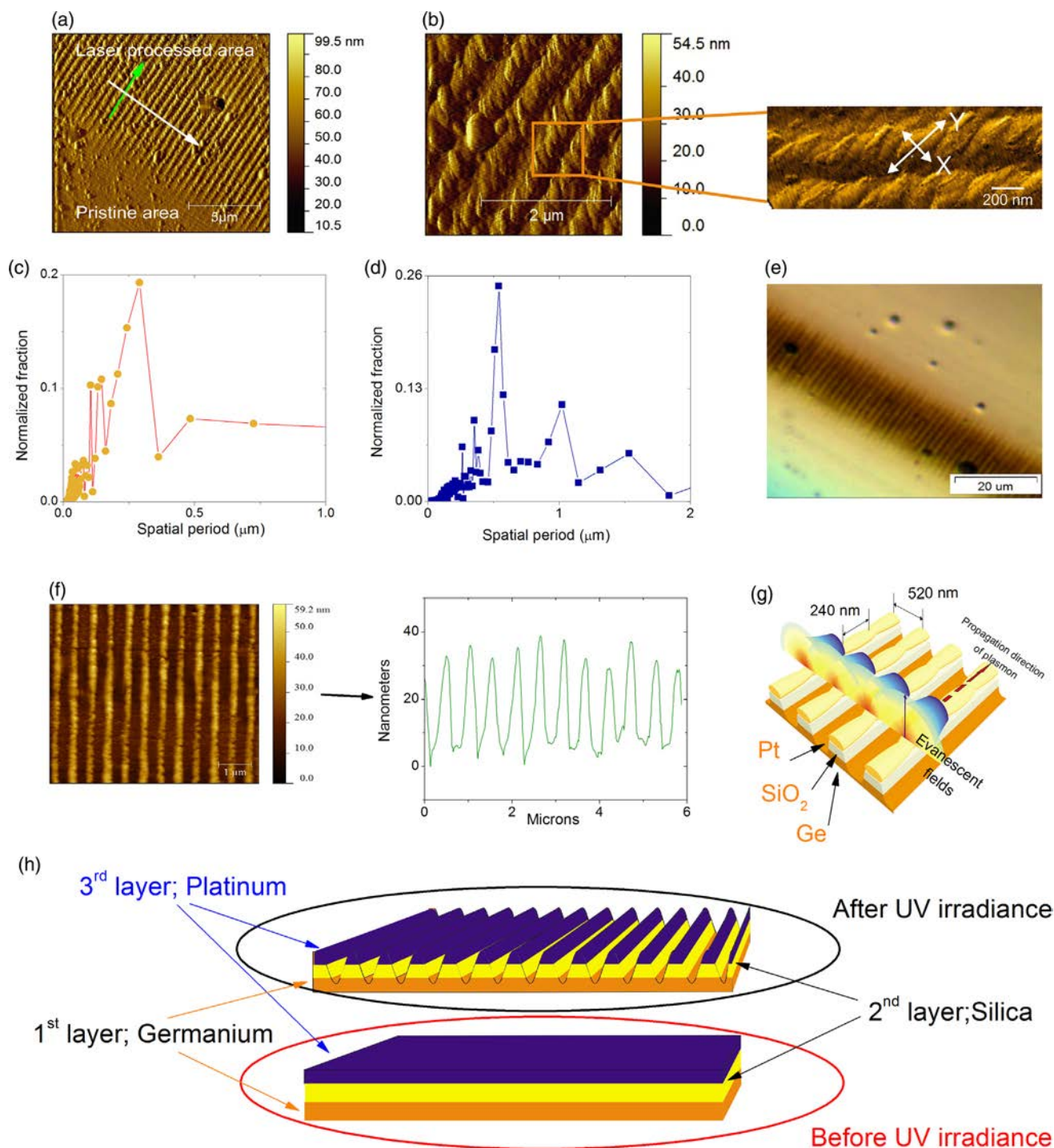
Figure 1. Surface profile characteristics of the fabricated samples. a) An AFM scan showing typical regions of pristine coating without UV-laser irradiation and UV-laser exposed area with nano-structuring. The arrows shows the two directions to evaluate spatial frequencies b) A high spatial resolution AFM scan showing the detail of the surface topology associated with each of the individual nano-antennas. The zoomed inset shows the fine structures inside the nano-antenna. c,d) Typical variation of the spatial frequencies along an individual nano-antenna and across the nano-antennas, respectively. e) A typical microscopic image of the processed BK7 glass. f) An AFM of a typical nano-antennae array on a planar 200 μm-thick BK7 substrate, along with a cross-section line profile of the AFM. g) Conceptual illustration of the mechanism of the optical conjoined SP array. h) Schematic of the fabrication procedure and materials used (Ge–SiO$_2$–Pt) for the plasmonic devices. Note: In all the cases, coating layers from bottom to top are 48 nm germanium, 48 nm silicon dioxide, and 32 nm gold, respectively.
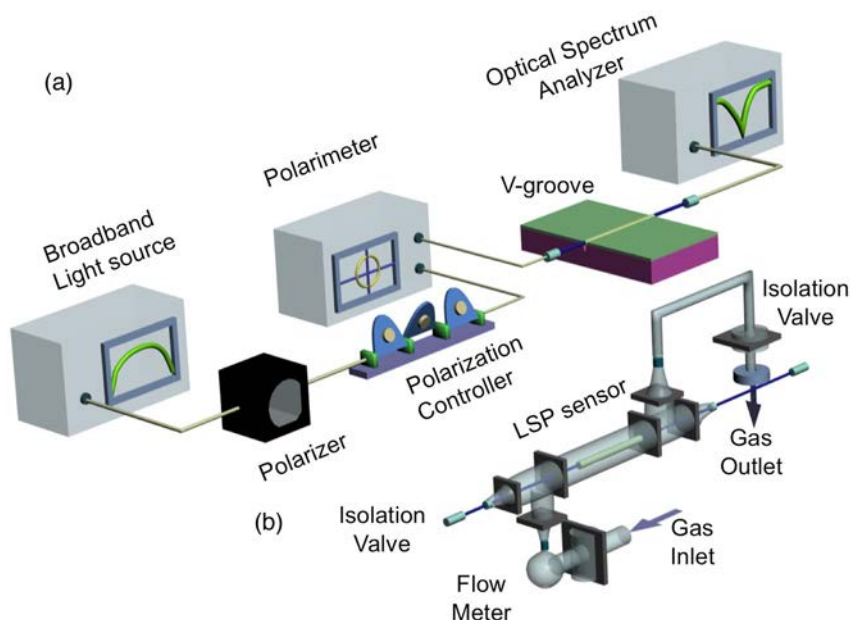
**ADVANCED
SCIENCE NEWS**

www.advancedsciencenews.com

**ADVANCED
PHOTONICS
RESEARCH**
Open Access

www.adpr-journal.com

Figure 2. Schematic of the experimental apparatus used to characterize the spectral response of LSP. a) Measurement facilities for liquid environment characterization. b) Experimental setup under pure gas condition. Note: An optimized maximum optical strength LSP resonance in the transmission spectrum was set as the starting point from a broadband light with controlled polarization.
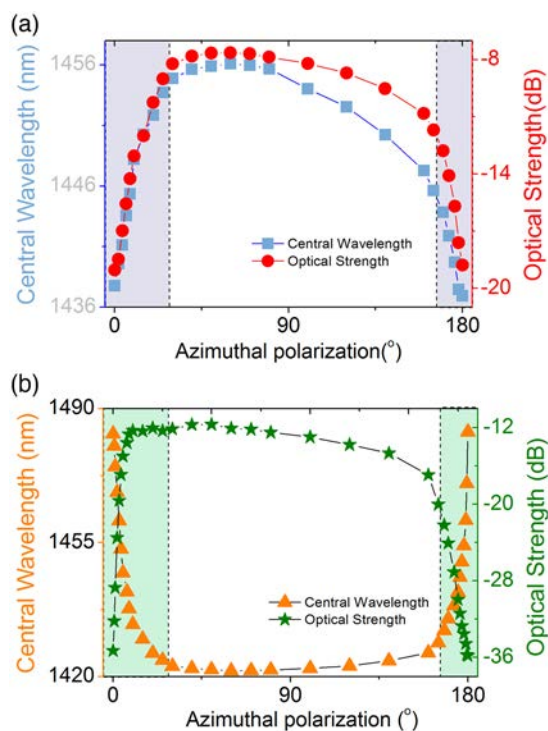

Figure 3. Typical optical spectral response of the SP with regard to polarization before and after UV-processing. a) The spectral response of conventional SP. b) The spectral response of LSP. Note: Shaded areas are high sensitivity regions.

nano-antennae. Furthermore, maximum RI sensitivities for the two metals used for the overlay were at different RI regimes,

which is expected due to their different optical properties. **Figure** 4a–h show the response in the aqueous and gaseous RI regime for two types of metal overlay, i.e., platinum and gold; the spectral wavelength shifts and thus the spectral sensitivity are determined using a centroid method;[26] more details given in Supporting Information.

The surface topology of the sensing platform dramatically modifies the plasmonic spectral behavior and sensitivity in response to changes in the surrounding RI. By altering the composition of the supporting metallic thin film, we can manipulate the surrounding index range in which a plasmon can be generated. For instance, in the aqueous regime, the variation of the transmission spectra for the platinum metal overlay coating as a function of surrounding RI, before and after UV-laser processing, are shown in Figure 4a,b, respectively. The spectral sensitivity extracted from these spectra increases slightly from $(2\text{–}3) \times 10^3 \, \text{nm} \, \text{RIU}^{-1}$ to $(4\text{–}6) \times 10^3 \, \text{nm} \, \text{RIU}^{-1}$ (Figure 4c) upon UV-laser processing. To obtain the maximum spectral sensitivity in the aqueous regime, the platinum metal overlay coating is replaced with gold due to the fact that optical properties of Au deliver a higher spectral sensitivity, as ascertained from the modeling. Figure 4d,e show how the transmission spectrum of the SP sensing platform changes using the gold overlay platform with respect to the surrounding RI. Similarly, Figure 4f shows the spectral response: wavelength shift and change in optical strength of the gold overlay device, before and after UV processing. Remarkably, the gold overlay produces a significant increase in sensitivity from an initial value around $100 \, \text{nm} \, \text{RIU}^{-1}$ to as much as $15 \times 10^3 \, \text{nm} \, \text{RIU}^{-1}$ following UV processing. This value is among the highest sensitivities reported in literatures in the aqueous index regime.[5,22,27]
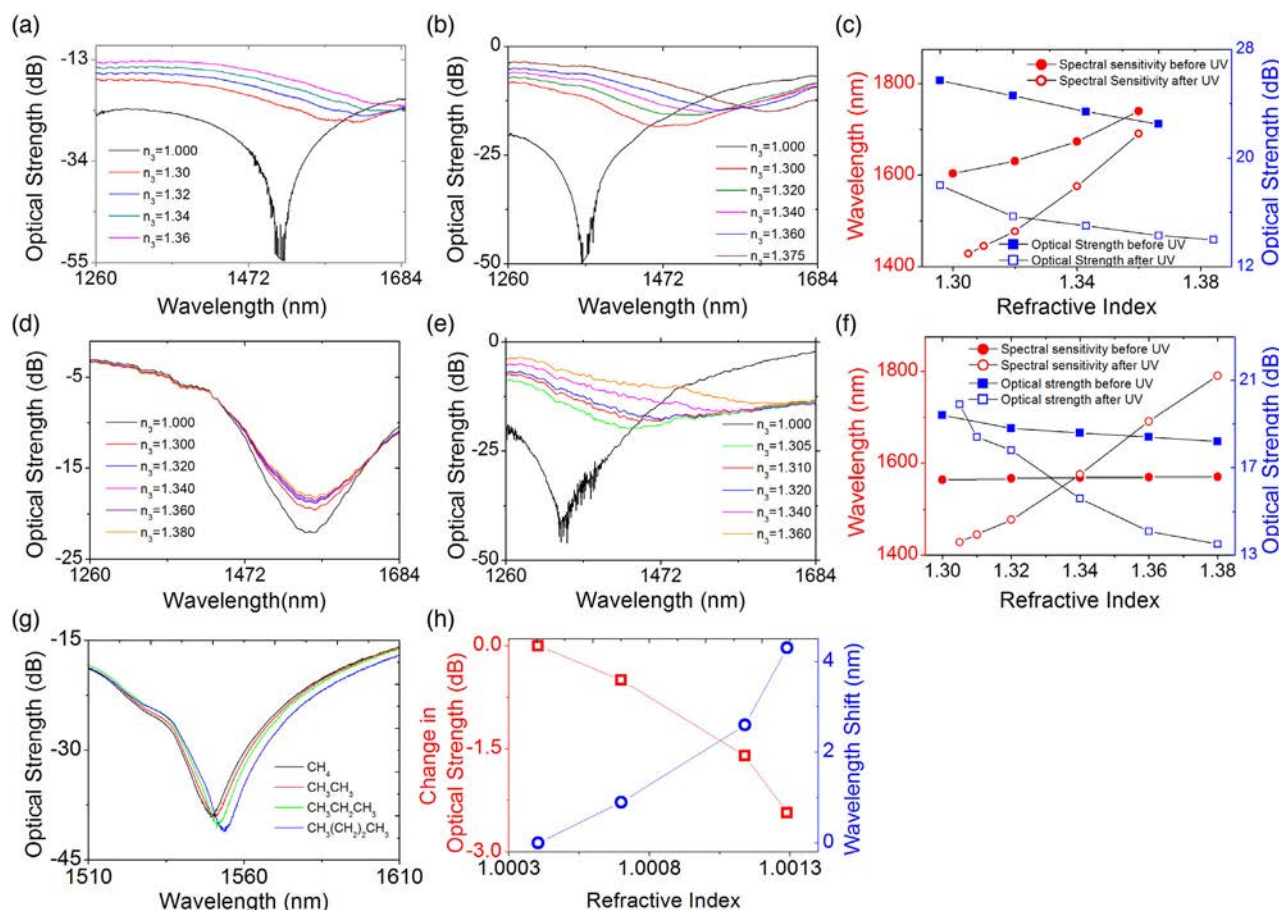
**ADVANCED
SCIENCE NEWS**

www.advancedsciencenews.com

**ADVANCED
PHOTONICS
RESEARCH**
Open Access

www.adpr-journal.com

Figure 4. Typical RI spectral shifts for two sensing platforms consisting of Ge-SiO2-Pt (GSP) and GSA multi-layer coatings in the aqueous and gaseous regime. Experimentally recorded spectra of the GSP a) before and b) after UV-laser processing. c) The obtained spectral sensitivity and optical strength of the GSP platform before and after UV-laser processing. Experimentally recorded spectra of the GSA platform d) before and e) after UV-laser processing. f) The obtained spectral sensitivity and optical strength of the GSA platform before and after UV-laser processing. Typical RI spectral responses for GSP in the alkane gases regime. g) Experimentally recorded transmission spectra and h) the obtained spectral index sensitivity.

The same experimental characterization was performed on devices for other applications and reported elsewhere.[5,22,25–28] A dramatic RI sensitivity increase, however, can be found in the gas regime from a typical value of $\approx$300 nm RIU^{-1} to $(4–30) \times 10^3$ nm RIU^{-1} after UV processing,[25] which has been utilized in detecting CO_2 and CH_4 via monitoring the changes in permittivity of carbon nanotubes and zinc oxide, respectively, due to oxidization/reduction chemical reactions.[25,28] An example of our plasmonic sensing platform operating in the gas regime, after UV processing, is shown in Figure 4g,h using the alkane gases. This yields typical sensitivity values of 11×10^3 and 5.5×10^3 dB RIU^{-1} with spectral noise having a standard deviation of $\Delta\lambda_{error} = 0.12$ nm and 0.1 dB. There are two important parameters that can be deduced from these results; the resolution defined as $\Delta\lambda_{error}/$(refractive index sensitivity; $S_{\lambda B}$) and the LOD. Note that LOD is dependent on the interrogation scheme, the light source spectral width, and the noise bandwidth of the measurement system. The LOD can be expressed in terms of standard deviation of the sensor noise output $\Delta\lambda_{error}$, bulk sensitivity defined as $S_{\lambda B} = \Delta\lambda/\Delta n_s$, and bandwidth of the spectral transmission feature of the SPs resonance $\Delta\lambda_{feature}$. Further-

more, there are 1000 discrete spectral data points per spectral scan (using an Agilent optical spectrum analyzer) across the resonant peak which yields a LOD $= \sqrt{((2 \cdot (\Delta\lambda\_feature + \Delta\lambda\_{-error}))/1000)/S_{\lambda B}}$. The full-width at a half-maximum of bandwidth resonances for the results given above is 34 nm. Thus yielding a gas index resolution of 2.2×10^{-5} RIU and 9.1×10^{-6} with LOD of 4.8×10^{-5} and 2.4×10^{-5} RIU for intensity and wavelength, respectively. Higher sensitivities are obtained using the same fabrication process for plasmonic sensing platform with a top-layer of platinum/zinc oxide yielding a wavelength spectral RI sensitivity of 1.5×10^5 nm RIU^{-1} and spectral bandwidth of 70 nm and with 0.06 nm standard deviation of noise yielding a maximum index resolution of 4.0×10^{-7} RIU in the gaseous regime.[28]

3. Modeling

To understand the underlying mechanism responsible for the experimental observations and to explain the ultra-high spectral sensitivities with respect to the RI of surrounding medium, two

theoretical approaches were used. First, via a combination of a conventional and well-established analytical model to predict the extinction spectrum of the constituent metal composite components of the nano-antenna as a function of wavelength[29] along with the effective dielectric medium, the Bruggeman effective medium approach[30] to estimate of their effective dielectric constants. This analytical modeling approach when used with spatial measurements of the constituent components of the nano-antenna that are referred to as "nano-blocks" yields reasonable agreement with the polarization dependence and the spectral tunabiltiy of the LSPs excitation resonances in the transmission spectrum of the sensing platform observed experimentally; see **Figure 5**. The assumptions and approximation used in the analytical modeling approach are given in the Supporting Information. Figure 5a shows the excitation of the LSPs given by the differing major and minor axes dimensions of the nano-blocks; *Y* and *X*. The definition of these two parameters can be seen in Figure 1b. The weakness of the analytical approach was in the prediction of spectral index sensitivities of the LSPs are too small by at least an order of magnitude; an example is shown in Figure 5c. This method yields sensitivities from 600–800 nm RIU^{-1}. In an attempt to replicate the observed experimental the ultra-high spectral index sensitivities, a numerical modeling approach as established.

To theoretically replicate the experimentally observed index spectral sensitivities, a second modeling approach is used. An FEM model was constructed consisting of 12 nano-antennas (total length of 6 μm) representing a small section of our sensing platform. The FEM is based upon the commercial software package COMSOL Multiphysics. The direction of the illuminating light is parallel to the stacking direction of this array; the excitation port being on the left-hand side with mesh size varying from 1.21×10^{-10} to 6.04×10^{-8} with a maximum element growth rate of 1.17 and full vector solution. This model is evaluated over a range of wavelengths from 1250 to 1750 nm, where the wavelength-dependent optical constants of the materials are incorporated for gold, silicon dioxide and germanium, according to the literature.[31] **Figure 6** shows an example of the electric field E_x and magnetic field H_z generated in the simulations. First, the amplitude of the *E*-field is shown in Figure 6a; this shows that *E*-fields overlap to adjacent nano-antenna. This overlap will affect the excitation of the electrons in each nano-antenna, thus creating

coupling between the SPs. This coupling to adjacent nano-atennae is more pronounced in the *x*-component of the *E*-field and that there is a collective coupling across the array; see Figure 6b. Furthermore, the majority of the H_z field associated with SP lies above the surface of the coating; see Figure 6c. Therefore, the propagation/interaction length of the SP has less dependency upon the roughness of the surface,[32,33] producing a long interaction length with the surrounding medium. Effectively, this antenna array, when optically irradiated in the infrared, creates infrared LSPs that are coupled and yielding an effective conjoint SP with an interaction length spanning over the entire array.

There are two factors that can be evaluated from the FEM numerical model that can be used to predict the ultra-high spectral index sensitivities that have been found experimentally (that yield ultra-low detection limits when used in conjunction with a bio-recognition molecule).[5,23] First, the dispersion of the LSPs over the wavelength range of interest from 1250–1750 nm is calculated from the results of FEM model run at a series of wavelength from 1250–1750 nm at increments of 50 nm. From this series of FEM simulations, the effective propagation constant of SPs is extracted at the various wavelength yielding $\Delta n_{LSR}/\Delta\lambda$. The authors would like to point out that the optical constants of the materials used in the FEM simulations at the various wavelengths came from the open literature.[31] The results from the series of runs of the FEM model are shown in Figure 6d,e. Second, we show the effective propagation constant of SPs as a function of the surrounding RI ($\Delta n_{LSR}/\Delta n_s$) at a specific wavelength λ_t, again; a series of FEM simulations were run over various refractive indices from 1.30 to 1.39 at all the wavelengths of interest; from 1250 to 1750 nm; the example is shown in Figure 6f at a wavelength of 1550 nm.

The first approximation for spectral index sensitivity is given by $(\Delta\lambda/\Delta n_s)|_{\lambda t} = (\Delta n_{LSR}/\Delta\lambda) \cdot (\Delta n_{LSR}/\Delta n_s)|_{\lambda t}$ for each of the individual SPs under the assumption that the dispersion relationship is linear around wavelength λ_t. Note that this basic model serves to estimate an overall magnitude for the anticipated sensitivity. Our numerically calculated sensitivities plotted in Figure 6g show a reasonable qualitative agreement with the experimental results for the mid-range values LSP order 11–13, with values ranging between 10^3 and 10^4 nm RIU^{-1}.

To understand the physical mechanism that creates these ultra-high spectral index sensitivities observed experimentally
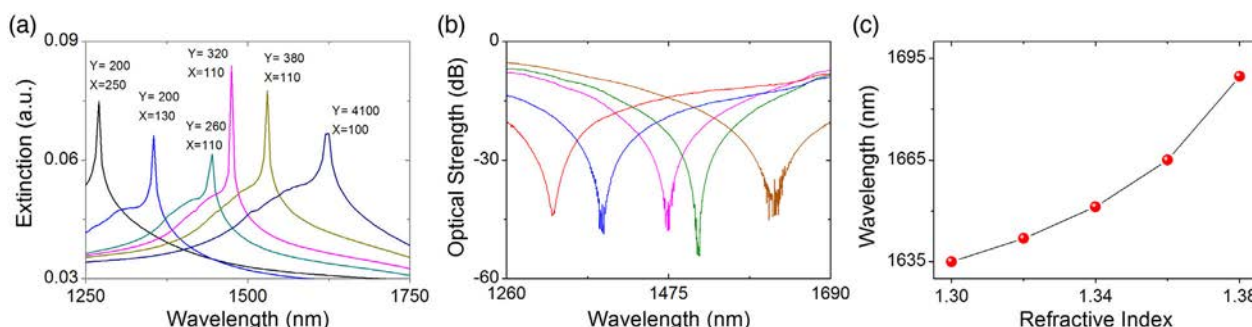

Figure 5. Analytical modeling of the LSP spectral responses. a) Typical calculated spectral shifts of the extinction of the LSP as a function of the spatial geometry and size of the nano-blocks, using the measured variation in the minor and major axes, for a GSA trilayer with a surrounding index of 1. b) Typical experimentally measured plasmon resonances, produced by varying the polarization of illuminating irradiance. c) Typical calculated RI sensitivity using minor and major axis values of 290 nm and 150 nm, respectively.
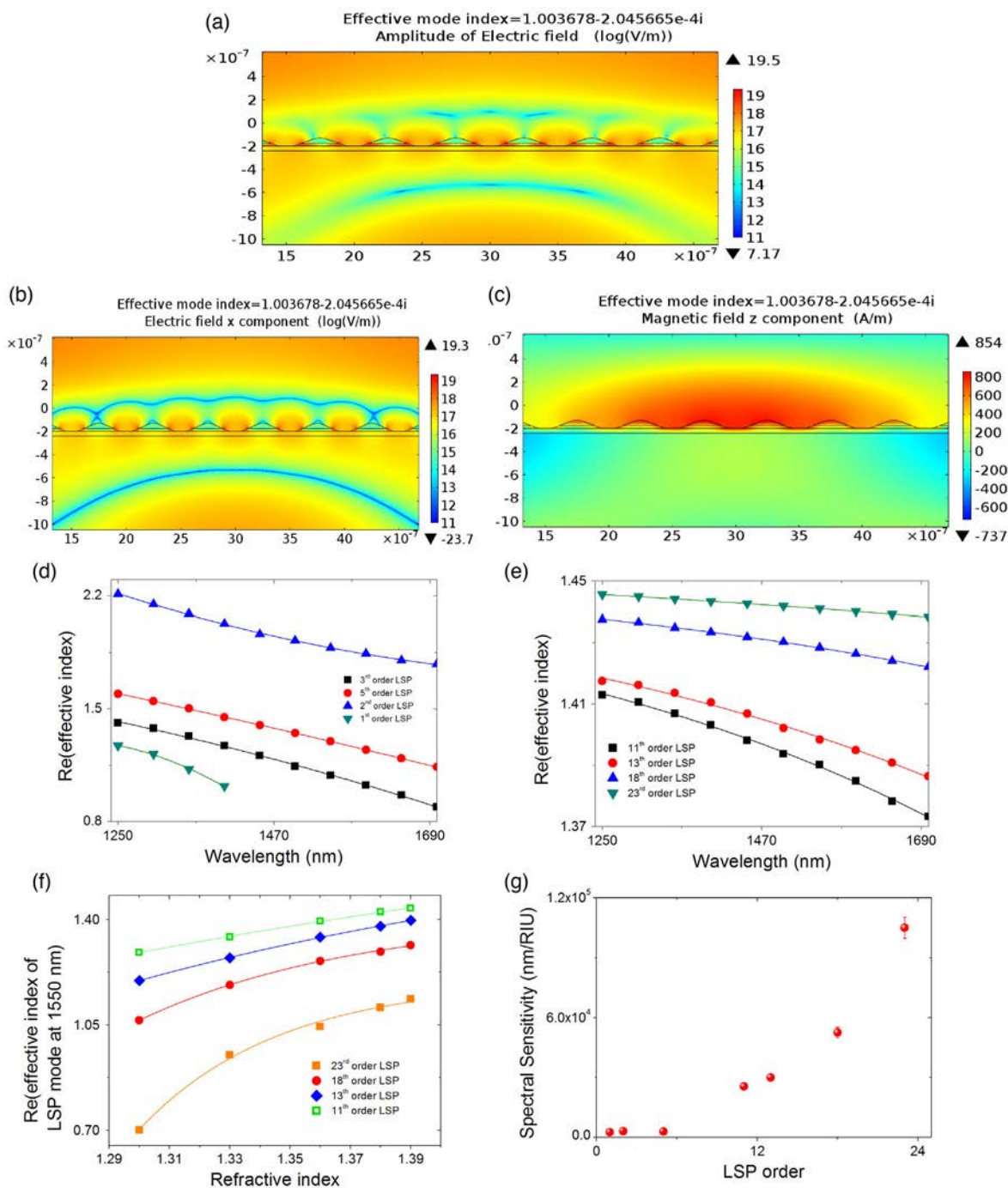
Figure 6. Numerical modeling of a section of the nano-antennae array generated conjoined LSP. FEM model showing the three major components, a) the overall amplitude of electric field, b) the *x*-component of the electric field, c) the *z*-component of the magnetic field at a wavelength of 1550 nm with a surrounding RI of 1.36. The physical dimensions are those measured experimentally using AFM. d) Calculated real part of RI for the dispersion relationship of the various orders of LSPs (1, 2, 3, 5, 11, 13, 18, 23). e) Zoom-in plot for the four higher orders. f) Real part of the effective index of the SPs, as a function of the surrounding medium's RI. g) Theoretical estimation of the spectral sensitivity of the SPs, as a function of plasmon order.

and the results obtained from the FEM numerical modeling, the propagation length needs to be inspected.

The FEM mode solutions for the propagation constants β are complex, thus describing a mode's effective wavelength and attenuation as it propagates. The propagation length is defined

as the distance a mode travels along the metal/medium interface; along the nano-antenna before decaying to e^{-1} of its original power, this is defined as $L_y = 1/2Im(\beta)$, assuming the radiative loss are small compared to intrinsic loss. The spatial location/ extension of the E_x field and the overall amplitude of the E field

spanning the array of nano-antennae producing a conjoint SP, lies above the surface and thus surface roughness is not significant. Moreover, the spatial location of the associated H_z field lies above the surface, again, indicating low-loss. These E/H fields are the perpendicular evanescent field to SP direction of travel along each nano-antenna. These perpendicular evanescent fields have an interaction length (decaying to e^{-1} of its original power) of 0.97 μm; this distance is greater than the distance between adjacent antennae which is 0.52 μm. These dimensions with respect to the size and spacing of individual nano-antenna and the overlap with the perpendicular evanescent fields, are visualized in **Figure 7**a. Furthermore, the "twisted rope like"

nano-antennae have a greater variation in the normal to their surface; thus perpendicular evanescent fields produced by an individual antenna occupy a greater volume of the wave vector space that is able to excitation/effect neighboring nano-antenna than a cylindrical-like nano-antenna; this is shown conceptual in Figure 7b.

Thus individual perpendicular evanescent fields created by the SP on a nano-antenna will overlap with adjacent nano-antenna that effects the SP generation and its own perpendicular evanescent fields. Creating a single collective response to an event on the order of a few millimeters, that is, combining a section of the array's SPs to produce a conjoint/overlay response of a number
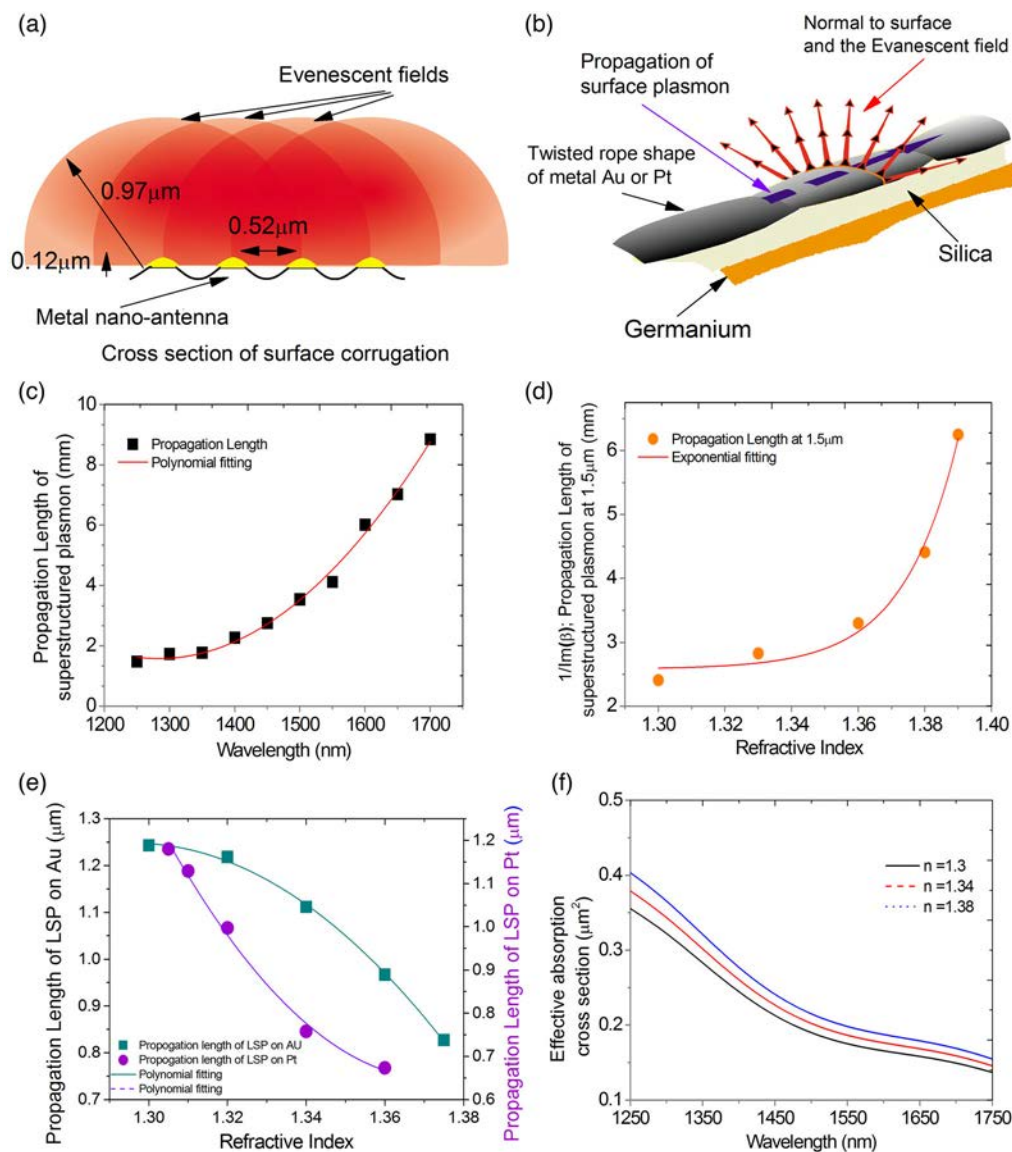

Figure 7. The physical characteristics of the LSPs calculated from the FEM numerical model and determined experimentally. a) The schematic cross-section view of the spatial extension of the evanescent field generated by the SPs. b) Conceptual illustration of the generation of evanescent field on the "twisted rope" surface of the nano-antennae. c,d) Effective propagation lengths of conjoined SP across the array (order 13) obtained from the FEM numerical modelling as a function of RI along with a fixed wavelength of 1550 nm and as wavelength with a fixed RI of 1.36 over the array of nano-antennae respectively. e) Experimentally determined propagation lengths along the nano-antennae for metals gold and platinum as a function RI, respectively. f) Coupling coefficients between adjacent evanescent fields on the nano-antennae.

of individual SPs. An example of the interaction length as a function of wavelength and as the surrounding RI in the infrared spectrum is shown in Figure 7b,c. Inspecting Figure 7b,c, we note the increasing propagation length with increasing wavelength is the same as conventional SP behavior, but opposite to the variation with increasing RI.[32] In this case, as the ambient surrounding RI increases, there is no energy flow increase in the metal due to the fact that the conjoint SP is above the surface and effectively there is no increase in the damping effect. The numerical results are compared to the experimentally determined propagation lengths of the SPs along the nano-antennae using the inverse proportionality relationship between propagation length and bandwidth of the SPR (Figure 6e).[34,35] Both metals used yielded propagation lengths of ranging from $0.7\,\mu m$ to $1.2\,\mu m$ over the range of RI used in the experiments. These experimental SP propagation length values are typical for the size of the nano-blocks within each nano-antenna. Moreover, these results are consistent with conventional LSPs having a decreasing propagation length with increasing RI. The interaction length/evanescent field generated by the SPs propagating along the nano-antennae, which spatially extends perpendicularly from the surface of the nano-antennae, can be calculated from the material constants. The two materials form the metal–dielectric interface at a given wavelength, with the RI of the surrounding medium given by $z_s = Im\left[\frac{\sqrt{(\varepsilon_m(\lambda)+n_s(\lambda)^2)\cdot\lambda}}{4\pi n_s(\lambda)^2}\right]$,[34] where $\varepsilon_\mu(\lambda)$ is the dielectric constant for either gold or platinum and $n_s(\lambda)$ is the medium's RI as a function of wavelength. Using the values given in the reference[31] yielded interaction length/evanescent field with spatial extensions from 0.85 to $0.95\,\mu m$ for gold nano-antennae over RI range of 1.3–1.38 and 0.48–$0.63\,\mu m$ for platinum nano-antennae over a RI range of 1.0–1.35. What this means is that the extension of the perpendicular evanescent field is larger than the separation of the individual nano-antenna, visualized in Figure 7a,e. The visualization of the overlap suggests coupling. Therefore, the coupling efficiency between adjacent fields and nano-antennae was investigated for the array at wavelengths range 1250–1750 nm. To estimate the coupling coefficients, several measured physical attributes of the nano-antennae needs to be used, such as, the spatial dimensions and using the assumption that the significant contribution to the excitation of the SP and thus the extinction spectrum is caused by irradiance absorption.[36] Individual nano-antennae are composed of smaller nano-blocks considering each of three axis of nano-blocks dependently; the coupling coefficients can be estimated between adjacent nano-antennas given by $C_{abs,i} \cong k Im[\alpha_i]$, where α_i is polarizability of the principle axis i and is given by $\alpha_i = 4\pi abc(\varepsilon_m(\lambda) - \varepsilon_s(\lambda)/3L_i$ $(\varepsilon_m(\lambda) - \varepsilon_s(\lambda)) + 3\varepsilon_s(\lambda))$, where a, b, and c are the values of the principle axis of the nano-antenna, which is assumed to be a cylindrical shape $a = b = 0.11\,\mu m$ and $c = 30\,\mu m$. The permittivity values $\varepsilon_m(\lambda)$ is for the supporting metal of the SP and $\varepsilon_s(\lambda)$ is the dispersion relationship of the surrounding medium. The parameter L_i is the form factor for the particular axis i with $L_a = \frac{1-\xi^2}{\xi^2}[\frac{1}{2\xi}\ln(1 + \xi/1 - \xi) - 1]$ and $L_b = L_c = \frac{1}{2}(1 - L_a)$, where the parameter ε is defined as $\xi = \sqrt{1 - (b/a)^2}$, producing coupling coefficient values from 0.15 to $0.42\,\mu m^2$ for this plasmonic platform. These are comparable values to other

nanostructures with strong coupling;[36,37] see Figure 7e. Thus, the conjoint plasmon is a type of strongly coupled "collective" SP. Therefore, as the evanescent field generated by a single nano-antenna is perturbed, the adjacent field is also affected due to the strong coupling. Thus the perturbation travels across the nano-antenna array, yielding an effective propagation across the array. Furthermore, this mechanism works with an array that has long-range order, from a few hundred micrometers to millimeters, for which part of the array can be seen in Figure 1e. It is known that the spectral sensitivity and wavelength shift are directly related to the degree of overlap integral of the evanescent fields in the sensing volume, which in turn is proportional to the interaction volume.[36,37] In addition, the[reisa]lso significantly increased interaction of the perpendicular evanescent field of the coupled adjacent SPs. The net effect of the aforementioned three factors is to yield an effective ultra-long propagation length traveling across and perpendicular to the nano-antennae. This leads to the experimentally observed significant increase in spectral sensitivity. Given that the shape and size of the individual elements of a nano-antenna play an important role in the dispersion of the plasmons, the sign of the wavelength shift may be reversed from this model.

4. Discussion and Conclusion

In comparison with the quoted values,[38] our experimentally determined RI spectral sensitivities obtained from our unique sensing platform are among the highest in the aqueous index regime (1.36–1.38) with sensitivity ranging from $4–6 \times 10^3\,nm\,RIU^{-1}$.[5,22] Moreover, the measured values are also among the highest in the gaseous index regime (1.0001–1.0015), from 5.5 to $15 \times 10^3\,nm\,RIU^{-1}$,[25,26,28] with figure-of-merit varying from 150 to 330.[28] The performance of this LSP sensing platform are compared to similar supporting substrates (optical fiber); see **Table 1**.

Inspecting Table 1, we observe that for the sensing platform reported here, sensitivities are approximately 3×10^4 to $1.5 \times 10^5\,nm\,RIU^{-1}$ in the gaseous regime from 1.0002–1.0014 that are ultra-high sensitivities. To make comparable comparisons to alterative sensing platforms, one needs to compare similar index regimes. Table 1 compares the aqueous index regime from 1.3 to 1.39, for which observe some of the highest reported sensitivities, approximately $10^4\,nm\,RIU^{-1}$.[39]

The sensitivities listed in the Table 1 are estimated from the data reported in the research article. Our basic numerical model offers realistic agreement with the experimental observations, offering further insight on the mechanism responsible for the experimental observed ultra-high sensitivities. The modeling also predicts that when optimized, this platform can offer spectral sensitivities ranging in excess of $10^5\,nm\,RIU^{-1}$, in the aqueous index regime. The aforementioned sensitivities can be achieved by further fine-tuning the fabrication technique in two ways. First, we require a reduction in the irregularities that can be perceived as "effective roughness" in the array topologies.[32,33] This would improve the repeatability of individual nano-antenna, which in turn improves the coupling of the LSPs. Furthermore, a decrease in this effective roughness would increase the interaction length (perpendicular evanescent field)

Table 1. Comparison nanostructured and localised plasmonic sensors.

Sensing platform description	Coating [nm]	Sensitivity [dB or nm RIU^{-1}]	Wavelength [nm]	Index range	Reference
Single mode fiber D-shaped Multilayered ordered nanowires	Ge, 48 and SiO$_2$, 48 and Pt, 36	1×10^4	1260–1680	1.33–1.39	[26]
Single mode fiber D-shaped Multilayered ordered nanowires	Ge, 48 and SiO$_2$, 48 and Ag, 32	1.2×10^4	1250–1680	1.3–1.39	[45]
Single mode fiber Multilayers, surface metallic grating	Ag, 43.3 and Au 1.2 nm	4000	400–1000	1.33	[48]
Multimode fiber , End-face nanospheres	Au, 35	2700	400–700	1.3–1.38	[49]
Single mode fiber Tilted FBG random nanowires	Ag, 20–50	175	1520–1610	1.33–1.365	[50]
Single mode fiber Tilted FBG random nanowires	Au, 50	651	1520–1600	1.330–1.347	[51]
Single mode fiber Tilted FBG nanowires	Ag, 30	1000	1520–1600	1.330–1.345	[52]
Single mode D-shaped etched to core fiber nanostrips	Au, 20	2×10^4	1400–1680	1.327–1.333	[39]
Single mode fiber bioconical taper, nanospheres	Au, 10.5	6000	400–1000	1.35	[53]
Multimode U-fiber, Triangular nanoparticles	Ag, 80–100	1116.8	300–600	1.334–1365	[54]

and thus increase the sensitivity. Second, improving the uniformity and controllability of the dimensions of the individual nano-antennae yields greater effective excitation of the higher modes, due to the fact that shape and size of the nano-antenna dominates the excitation of the SPs.[40] When assuming similar standard deviation of noise within the sensor, the scheme yields typical RI resolution of 4.0×10^{-8} RIU (by improvements in the interrogation scheme) and higher in the aqueous index regime. Investigations are underway to predict the correct optical illumination requirements and refinement of the shape of the nano-antenna to have an optimized coupling efficiency to higher order SPs, thereby yielding even higher sensitivities. The flexibility of this direct-write fabrication procedure (on any substrates with flat surfaces) offers the opportunity to produce more complex nano-pattern surface structures.

In conclusion, we have proposed and demonstrated a new mode of operation for SPs to create a collective state of a number of LSP or an effective conjoint SP spanning over a section of the sensing array. We have shown theoretically and experimentally that there is a significant increase in the interaction length (perpendicular evanescent field or referred to as the scattered radiation field) of LSP due to strong coupling between adjacent nano-antennae. In addition, the "conjoint surface plasmon mode" exists due to the close proximity of other nano-antennae and the surface topologies of the "nano-blocks" within each nano-antennae at the wavelength of excitation. These physical attributes of the nano-antennae result in strong coupling between the spatial location of the SP. Furthermore, the fact that nano-antenna arrays have long-range ordering and have low effective roughness yielded the ultra-high sensitivities. Furthermore, comparing this mode operation to plasmonic surface lattice resonances,[41] the resonances are much narrower than the observed LSPs in these experiments. In addition, and more importantly, that the spectral index sensitivity of the plasmonic surface lattice resonances are much less (≈ 400 nm RIU^{-1}) which is more than order of magnitude less than the purposed conjoint SP. Moreover, considering using the near-field or far-field diffractive coupling effects as the mechanism for the observed SPs would produce a narrowing of the bandwidth of

the resonance of the SP which is not observed experimentally. Also, the diffractive coupling effect can produce a splitting of the SP resonances in transmission spectra which is not observed in the experiments conducted; examples are shown in Figure 4.

This unique operational mode of SPs has great potential to make direct experimental observations and help answer more fundamental questions on the physical dynamics of proteins and the opportunities to explore the mutual interaction between biological components and surfaces.[42] Such operational mode may also offer the real possibility of many new applications, such as, the experimental real-time study of single bimolecular binding kinetics, detection of ultra-low concentration (below the fM level) of proteins and small molecules for the early diagnosis of various diseases.[43,44]

5. Experimental Section

Fabrication of the Optical Sensing Platform: Initially, the formation of structures via the interaction of the germanium oxides on exposure to UV laser illumination were investigated using planar substrates. A thin-film coating of germanium with a thickness of 48 nm was deposited upon a BK7 glass substrate with a thickness of 150 μm. The reason for using a thickness of 48 nm of germanium comes from the previous work[45] and the results have been published in the previous studies.[46] Furthermore, this effect was utilized in the formation of multi-layered, 2D nano-structured films that supported the LSPs. The multi-layered thin films consisted of three different materials (germanium (48 nm), silicon dioxide (48 nm), and metal overlay coating of varying thickness (Pt; 28 nm), (Au; 32 nm), (Ag; 32 nm) producing a planar surface. For ease of interrogation of the SP, a D-shaped single-mode optical fiber as the optical waveguide and supporting substrate. The D-shaped fibers were fabricated from a standard telecoms optical fiber (SMF28) by mechanically lapping and polishing the optical fiber with the flat area 3 μm from the core/cladding interface (Phoenix Photonics Ltd, UK). The thin films of germanium and other thin films were deposited using an RF sputtering machine (Nordico 6 in. RF/DC 3 target excitation machine, Nordiko 6, Nordiko Technical Services Limited, Havant, Hampshire, UK).

Second, the germanium-coated planar substrates were mounted, aligned, and exposed to various intensities of 244 nm laser light. Note that the opto-mechanical arrangement of the apparatus was the same as used for the UV laser inscription of optical fiber gratings.[47] The UV light source was an argon ion, continuous wave laser (INNOVA Sabre Coherent Inc.)

**ADVANCED
SCIENCE NEWS**

www.advancedsciencenews.com

**ADVANCED
PHOTONICS
RESEARCH**

www.adpr-journal.com

producing 500 mW at 244 nm. The laser beam was focused along the line of travel of the air-bearing stage (using a plano-convex lens with a focal length of 80 mm) and then passed through a phase mask (period of 1.018 µm, a QPS phase mask). The beam was focused perpendicularly to the line of travel of the air-bearing stage (Aerotech Inc.) with further alignment of beam to be constantly focused on the surface of the sample (using an additional plano-convex lens having focal length of 80 mm). A schematic of the coating process to realize the low-dimensional nanostructure is shown in Figure 1h.

Supporting Information

Supporting Information is available from the Wiley Online Library or from the author.

Conflict of Interest

The authors declare no conflict of interest.

Author Contributions

T.A. developed the original plasmonic concept. T.A. modeled, designed, and performed experiments, analyzed the data for the plasmonic devices. T.A., C.M., C.W., R.N. fabricated the plasmonic devices. Characterization of sensing platform and experiments performed by V.K. T.A., K.K., and C.W. The manuscript was written by T.A., C.M., P.D., K.K., D.J.W., R.N., X.L., P.C., and J.D.A-C. All authors discussed the results and commented on the manuscript.

[1] J. N. Anker, W. P. Hall, O. Lyandres, N. C. Shah, J. Zhao, R. P. Van Duyne, *Nat. Mater.* **2008**, *7*, 442.

[2] S. Y. Ding, J. Yi, J. F. Li, B. Ren, D. Y. Wu, R. Panneerselvam, Z. Q. Tian, *Nat. Rev. Mater.* **2016**, *1*, 16021.

[3] S. I. Bozhevolnyi, V. S. Volkov, E. Devaux, J. Y. Laluet, T. W. Ebbesen, *Nature.* **2006**, *440*, 508.

[4] M. Hu, J. Y. Chen, Z. Y. Li, L. Au, G. V. Hartland, X. D. Li, M. Marquez, Y. N. Xia, *Chem. Soc. Rev.* **2006**, *35*, 1084.

[5] T. Allsop, C. Mou, R. Neal, S. Mariani, D. Nagel, A. Poole, K. Kalli, A. Hine, D. J. Web, P. Culverhouse, M. Mascini, M. Minunni, I. Bennion, *Opt. Express* **2017**, *25*, 39.

[6] V. Lirtsman, M. Golosovsky, D. Davidov, *J. Appl. Phys.* **2008**, *103*, 014702.

[7] A. V. Kabashin, P. Evans, S. Pastkovsky, W. Hendren, G. A. Wurtz, R. Atkinson, R. Pollard, V. A. Podolskiy, A. V. Zayats, *Nat. Mater.* **2009**, *8*, 867.

[8] H. Wei, S. M. H. Abtahi, P. J. Vikesland, *Environ. Sci. Nano.* **2015**, *2*, 120.

[9] Z. Liang, J. Sun, Y. Jiang, L. Jiang, X. Chen, *Plasmonics* **2014**, *9*, 859.

[10] J. Leuthold, C. Hoessbacher, S. Muehlbrandt, A. Melikyan, M. Kohl, C. Koos, W. Freude, *Opt. Photon. News* **2003**, *24*, 28.

[11] S. W. Lee, K. S. Lee, J. Ahn, J. J. Lee, M. G. Kim, Y. B. Shin, *ACS Nano* **2011**, *5*, 897.

[12] J. H. Seo, J. H. Park, S. I. Kim, B. J. Park, Z. Ma, J. Choi, B. K. Ju, *J. Nanosci. Nanotechnol.* **2014**, *14*, 1521.

[13] P. Y. Chen, A. Alù, *Phys. Rev. B.* **2010**, *82*, 235405.

[14] L. Novotny, N. Van Hulst, *Nat. Photonics.* **2011**, *5*, 83.

[15] G. Sadashivappa, N. Sharvari, *Int. J. Renew. Energy Technol. Res.* **2015**, *4*, 1.

[16] F. J. Garcia-Vidal, L. Martin-Moreno, J. B. Pendry, *J. Opt. A: Pure Appl. Opt.* **2005**, *7*, S97.

[17] W. Dickson, G. Wurtz, P. Evans, D. O'Connor, R. Atkinson, R. Pollard, A. V. Zayats, *Phys. Rev. B.* **2007**, *76*, 115411.

[18] E. Petryayeva, U. J. Krull, *Anal. Chim. Acta* **2011**, *706*, 8.

[19] A. J. Haes, R. P. Van Duyne, *J. Am. Chem. Soc.* **2002**, *124*, 10596.

[20] Z. Liu, A. Boltasseva, R. H. Pedersen, R. Bakker, A. V. Kildishev, V. P. Drachev, V. M. Shalaev, *Metamaterials* **2008**, *2*, 45.

[21] O. Muskens, V. Giannini, J. Sanchez-Gil, J. Gomez Rivas, *Nano Lett.* **2007**, *7*, 2871.

[22] T. Allsop, R. Neal, C. Wang, D. A. Nagel, A. V. Hine, P. Culverhouse, J. D. A. Castanon, D. J. Webb, S. Scarano, M. Minuni, *Biosens. Bioelectron.* **2019**, *135*, 102.

[23] V. B. Neustruev, *J. Phys.: Condens. Matter* **1994**, *6*, 6901.

[24] S. H. Wemple, M. Didomenico, *Phys. Rev. B.* **1970**, *1*, 193.

[25] T. Allsop, R. Neal, E. M. Davies, C. Mou, P. Brown, S. Rehman, K. Kalli, D. J. Webb, P. Calverhouse, I. Bennion, *Meas. Sci. Technol.* **2010**, *21*, 094029.

[26] T. Allsop, R. Arif, R. Neal, K. Kalli, V. Kundrát, A. Rozhin, P. Culverhouse, D. J. Webb, *Light: Sci. Appl.* **2016**, *5*, e16036.

[27] T. Allsop, R. Neal, C. Mou, P. Brown, S. Saied, S. Rehman, K. Kalli, *Appl. Opt.* **2009**, *48*, 276.

[28] T. Allsop, V. Kundrat, K. Kalli, G. B. Lee, R. Neal, P. Bond, B. G. Shi, J. Sullivan, P. Culverhouse, D. J. Webb, *Sens. Actuators B* **2018**, *255*, 843.

[29] V. A. Markel, *JOSA A* **2016**, *33*, 71244.

[30] D. Aspnes, J. Theeten, F. Hottier, *Phys. Rev. B.* **1979**, 3292.

[31] E. D. Palik, *Handbook Of Optical Constants Of Solids*, Vol. 3, Academic press, London **1998**.

[32] A. Kolomenski, A. Kolomenskii, J. Noel, S. Peng, H. Schuessler, *Appl. Opt.* **2009**, *48*, 5683.

[33] A. V. Zayats, I. I. Smolyaninov, A. A. Maradudin, *Phys. Rep.* **2005**, *408*, 131.

[34] K. Johansen, H. Arwin, I. Lundstrom, B. Liedberg, *Rev. Sci. Instrum.* **2000**, *71*, 3530.

[35] E. M. Yeatman, *Biosens. Bioelectron.* **1996**, *11*, 635.

[36] A. Shalabney, I. Abdulhalim, *Laser Photon. Rev.* **2011**, *5*, 571.

[37] A. I. Vkäeväinen, R. J. Moerland, H. T. Rekola, A.-P. Eskelinen, J.-P. Martikainen, D.-H. Kim, P. Törmä, *Nano Lett.* **2013**, *14*, 1721.

[38] A. Leung, P. M. Shankar, R. Mutharasan, *Sens. Actuators B* **2007**, *125*, 688.

[39] Y. J. He, *Opt. Express* **2013**, *21*, 23498.

[40] K. L. Kelly, E. Coronado, L. L. Zhao, G. C. Schatz, *J. Phys. Chem. B* **2003**, *107*, 668.

[41] V. G. A. V. KravetsKabashin, A. V. Kabashin, W. L. Barnes, A. N. Grigorenko, *Chem. Rev.* **2018**, *118*, 5912.

[42] J. Grunenberg, *Phys. Chem. Chem. Phys.* **2011**, *13*, 10136.

[43] J. W. Scannell, J. Bosley, *PLoS One* **2016**, *11*, e0147215.

[44] D. L. Mobley, K. A. Dill, *Structure* **2009**, *17*, 489.

[45] T. Allsop, R. Neal, C. Mou, K. Kalli, S. Saied, S. Rehman, D. J. Webb, P. F. Culverhouse, J. L. Sullivan, I. Bennion, *IEEE J. Quantum Electron.* **2012**, *48*, 394.

[46] T. Allsop, R. Neal, V. Kundrát, C. Wang, C. Mou, P. Culverhouse, J. D. Ania-Castanon, K. Kalli, D. J. Webb, *Optics Lett.* **2019**, *44*, 195.

[47] R. Kashyap, *Fiber Bragg Gratings*, Academic Press, Cambridge, MA **2009**.

[48] E. M. Hicks, O. Lyandres, W. P. Hall, S. Zou, M. R. Glucksberg, R. P. Van Duyne, *J. Phys. Chem. C* **2007**, *111*, 4116.

[49] B. Lee, S. Roh, H. Kim, J. Jung, in *Proc. of the Photonic Fiber and Crystal Devices: Advances in Materials and Innovations in Device Applications*, International Society for Optical Engineering, San Diego, CA **2009**.

[50] H. H. Jeong, N. Erdene, J. H. Park, D. H. Jeong, H. Y. Lee, S. K. Lee, *Biosens. Bioelectron.* **2013**, *39*, 346.

[51] A. Bialiayeu, A. Bottomley, D. Prezgot, A. Ianoul, *J. Nanotechnol.* **2012**, *23*, 444012.

[52] J. M. Renoirt, M. Debliquy, J. Albert, A. Ianoul, C. Caucheteur, *J. Phys. Chem. C* **2014**, *118*, 11035.

[53] S. Kumar, B. K. Kaushik, R. Singh, N. K. Chen, Q. S. Yang, X. Zhang, W. Wang, B. Zhang, *Biomed. Opt. Express* **2019**, *10*, 2150.

[54] H. Song, H. Zhang, Z. Sun, Z. Ren, X. Yang, Q. Wang, *AIP Adv.* **2019**, *9*, 085307.